Frontiers in Earth Science

TYPE Original Research
PUBLISHED 16 January 2023
DOI 10.3389/feart.2022.1031985

In situ stress distribution law of fault zone in tunnel site area based on the inversion method with optimized fitting conditions

Tiansheng Li[1,2], Ziquan Chen[1], Zihan Zhou[1]* and Yeming Bao[2]

[1]Key Laboratory of Transportation Tunnel Engineering, Ministry of Education, Southwest Jiaotong University, Chengdu, Sichuan, China, [2]China Railway 12th Bureau Group Co., Ltd., Taiyuan, Shanxi, China

OPEN ACCESS

EDITED BY
Lei-Lei Liu,
Central South University, China

REVIEWED BY
Zhendong Leng,
Gezhouba Explosive, China
Fuqiong Huang,
China Earthquake Networks Center,
China

*CORRESPONDENCE
Zihan Zhou,
zihanzhou@my.swjtu.edu.cn

SPECIALTY SECTION
This article was submitted to Environmental Informatics and Remote Sensing, a section of the journal Frontiers in Earth Science

RECEIVED 30 August 2022
ACCEPTED 26 October 2022
PUBLISHED 16 January 2023

CITATION
Li T, Chen Z, Zhou Z and Bao Y (2023), In situ stress distribution law of fault zone in tunnel site area based on the inversion method with optimized fitting conditions.
Front. Earth Sci. 10:1031985.
doi: 10.3389/feart.2022.1031985

COPYRIGHT
© 2023 Li, Chen, Zhou and Bao. This is an open-access article distributed under the terms of the Creative Commons Attribution License (CC BY). The use, distribution or reproduction in other forums is permitted, provided the original author(s) and the copyright owner(s) are credited and that the original publication in this journal is cited, in accordance with accepted academic practice. No use, distribution or reproduction is permitted which does not comply with these terms.

Tunnel construction in high geo-stress strata faces the risk of extreme natural disasters such as large squeezing deformation and rockburst. Therefore, it is of great significance to adopt a high-precision inversion method to investigate the distribution law of *in situ* stress in the tunnel site area. In this paper, the *in situ* stress inversion research was carried out based on a plateau tunnel with a buried depth of more than 1000 m. The idea of improving the inversion accuracy by unifying displacement constraints was proposed by aiming at the defects of the traditional method on the boundary conditions. Furthermore, the impact of the constant term in the regression model on the fitting accuracy was discussed. According to the inversion method with optimized fitting conditions, the *in situ* stress distribution characteristics in the tunnel site area were obtained, and the variation law of the *in situ* stress near the fault zone was discussed. The results showed that after unifying displacement constraints, the comprehensive inversion accuracy comprehensive indicator reflecting the inversion accuracy decreased from 15.291 to 12.895, indicating that the inversion error was effectively controlled. Whether the constant term should be retained had a random effect on the inversion accuracy, so it was recommended that this issue be independently verified when fitting the data. When approaching the inner side of the fault from the outer side, the *in situ* stress first increased slightly and then decreased significantly. Moreover, the wider the fault impact zone and the farther the fault distribution distance, the more significant the amplitude of stress change, e.g., the maximum amplitude of stress change reached 9.0 MPa. In addition, the *in situ* stress orientation near the fault can be significantly deflected. And the wider the fault impact zone, the more pronounced the deflection.

KEYWORDS

tunnel engineering, deep-buried tunnel, *in situ* stress, fault zone, inversion method

1 Introduction

Affected by the intense tectonic movements of the Indian Ocean and the Eurasian plates, the Qinghai-Tibet Plateau has natured many faults and high tectonic *in situ* stress (Zhang D. L. et al., 2022; Wang et al., 2022). Tunnel project constructed in this stratum faces the significant risk of geological disasters, such as squeezing large deformation disasters in soft rock (Hu et al., 2022; Liu et al., 2022) and rockburst disasters in hard rock (Fan et al., 2021; Zhang H. et al., 2022). Therefore, it is significant to investigate the *in situ* stress distribution law in deep-buried tunnels crossing fault zone strata to guide the structural design and prevent and control geological disasters.

Since there are no conditions for measuring inside the tunnel in the geological exploration stage, the hydraulic fracturing method is the only means to measure the *in situ* stress in this stage (Zhang et al., 2014). The multiple linear regression method developed based on the elastic stress assumption of the hydraulic fracturing method is one of the commonly used methods for *in situ* stress inversion (Zhang et al., 2012). Figueiredo et al. (2014) used the multiple linear regression method to reveal that the *in situ* stress of the granite formation of a hydropower station in northern Portugal was controlled by self-weight stress and shear stress. Li et al. (2015) proposed the local least squares regression measure to improve the inversion accuracy based on the multiple linear regression method and applied it to a dam project. Meng et al. (2020) adopted the multiple linear regression method to put forward the idea of *in situ* stress inversion for high geo-temperature tunnels considering the temperature stress component. Based on the multiple linear regression method, Xu et al. (2021) proposed an *in situ* stress inversion system that comprehensively considered information such as geological tectonic background and topography. Meng et al. (2021) discussed the effect of using ridge regression to improve the inversion accuracy of the multiple linear regression method. However, the displacement constraints of each calculation condition in these applications are not strictly consistent, likely leading to significant inversion errors.

Some scholars have revealed the *in situ* stress distribution law in tectonic strata based on the inversion results. Han et al. (2016) found no direct linear relationship between the horizontal tectonic stress and the burial depth in the syncline, and the stress orientation was deflected inside and outside the syncline. Li G. et al. (2020) studied the distribution law of *in situ* stress in gully strata relying on a hydropower station in the mountainous area of southwest China, and the conclusion showed that buried depth had a positive effect on the *in situ* stress level. Based on the *in situ* stress inversion results of tunnel engineering of the Sichuan-Tibet Railway, Li X. P. et al. (2020) concluded that the *in situ* stress dropped suddenly inside the fault. Ning et al. (2021) studied the *in situ* stress distribution characteristics in the valley area considering geological tectonic movement and river erosion and believed that the stress relaxation effect occurred in the unloading and rebound area of the slope. Zhou et al. (2022) studied the *in situ* stress distribution law of the intrusive rock strata through the segmented inversion method and believed that there was a sudden stress change phenomenon at the intrusive rock interface. However, although these studies have investigated the *in situ* stress distribution of some structural strata, few studies have systematically analyzed the *in situ* stress distribution characteristics of dense fault zones.

Relying on a deep-buried Plateau tunnel in Southwest China, this paper first analyzed the optimization effect of unified displacement constraints on inversion accuracy. Then, the random effect of the constant term in the regression model on the inversion error was discussed. The *in situ* stress distribution law when the tunnel crosses the fault zone was revealed based on the multiple linear regression method with optimized fitting conditions. Furthermore, the change law of the value and orientation of the *in situ* stress near the fault was emphatically discussed.

2 Engineering background and measured *in situ* stress

2.1 Engineering background

The plateau tunnel is located on the eastern edge of the Qinghai-Tibet Plateau, passing through Zheduo Mountain, the first high mountain in Sichuan Province to enter Tibet. Its south is the Indian Ocean plate, and its north is the Eurasian plate. The plate compression has created an active neotectonic movement in this area (Figure 1). Affected by the intense geological tectonic action, the tunnel site area is densely covered with mountains and ravines. Figure 1B shows the typical plateau landform characteristics of the tunnel site area, and its surface elevation is about 3460–4730 m. In addition, the strong stratigraphic cutting action formed the famous Y-shaped active fault zone in southwest China near the tunnel site. The tunnel is located on the Xianshuihe active fault zone on the northwest side of this area (Figure 1D).

The tunnel entrance is in Zheduotang Village, and its exit is in Shuiqiao Village. Its total length and maximum buried depth are about 20.8 km and 1215 m, respectively (Figure 2). The strata traversed by the tunnel include quartz sandstone, biotite adamellite, and slate. Affected by the Xianshuihe active fault zone, 12 faults are distributed in the tunnel site area. Among them, the Zheduotang fault covers the range of 3–4 km in the entrance, which is only represented by the actual strata. Among them, the faults with a wider impact range include the Zheduotang branch fault with a width of 302 m, the Jinlongsi-mozigou fault with a width of 198 m, the F15 fault with a width of 296 m, and the Yulongxi fault with a width of 614 m. Besides, the rest of the faults are roughly 100 m wide.

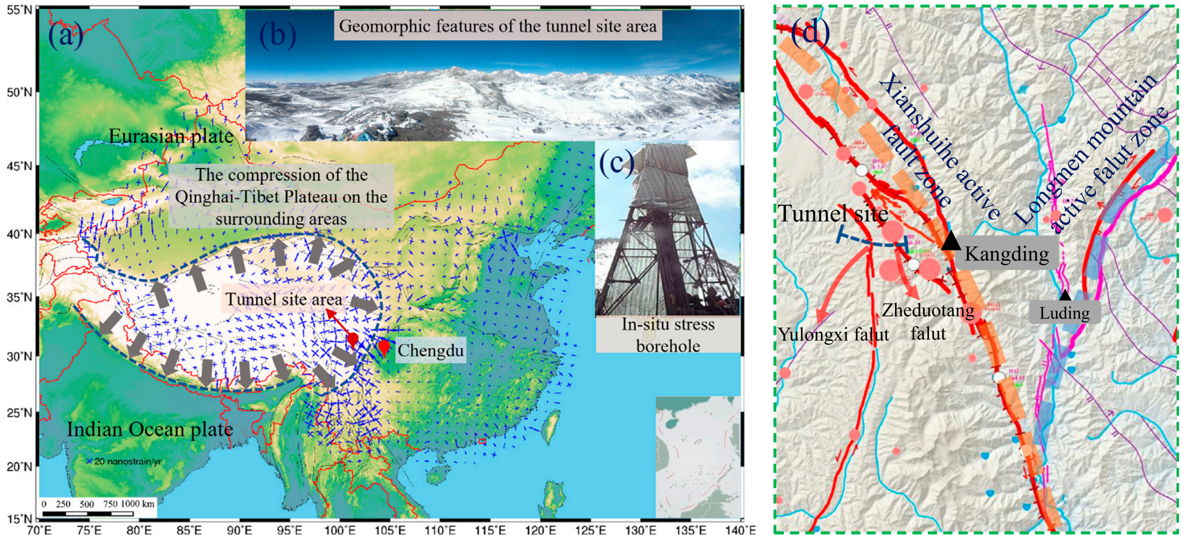

FIGURE 1
Geological background of the tunnel: **(A)** stress field of China; **(B)** plateau landform characteristics; **(C)** *in situ* stress measurement; **(D)** main fault zone around tunnel site.

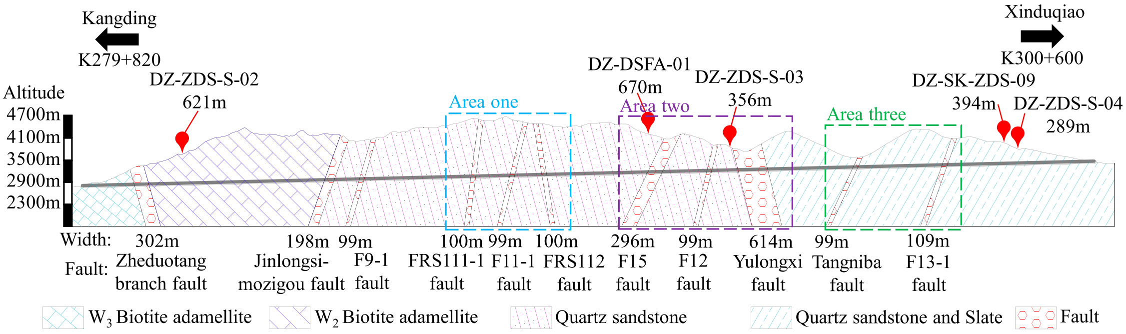

FIGURE 2
Longitudinal profile of the tunnel.

2.2 Measured *in situ* stress

The large buried depth and complex tectonic geological environment are typic features of the tunnel. Generally, in addition to the self-weight stress, there is a nonnegligible horizontal tectonic stress in the strata with active geological movement (Yuan et al., 2022). Furthermore, in this geological environment, the horizontal tectonic stress is even greater than the vertical self-weight stress (Zhao et al., 2021). In order to investigate the *in situ* stress distribution characteristics in the tunnel site area, field measurement was carried out by the hydraulic fracturing method during the geological exploration stage. There are five *in situ* stress boreholes in total. Among them, the maximum depth of DZ-ZDS-S-02, DZ-DSFA-01, DZ-ZDS-S-03, DZ-SK-ZDS-09, and DZ-ZDS-S-04 boreholes is 621 m, 670 m, 356 m, 394 m, and 289 m, respectively (Figure 2). Except for the DZ-DSFA-01 borehole, which has five measuring points, the other boreholes have four.

Figure 3 shows the measured *in situ* stress at different measuring points of each borehole. It can be seen that for a single borehole, the *in situ* stress of each measuring point increases almost linearly with the increase of the buried depth. Especially the vertical stress (σ_V), the measured *in situ* stress of all boreholes maintains the same linear growth relationship. On the other hand, the maximum horizontal principal stress (σ_H) and the minimum horizontal principal stress (σ_h) between different boreholes show an apparent nonlinear relationship. Among them, the DZ-ZDS-S-02, DZ-SK-ZDS-09, and DZ-ZDS-S-

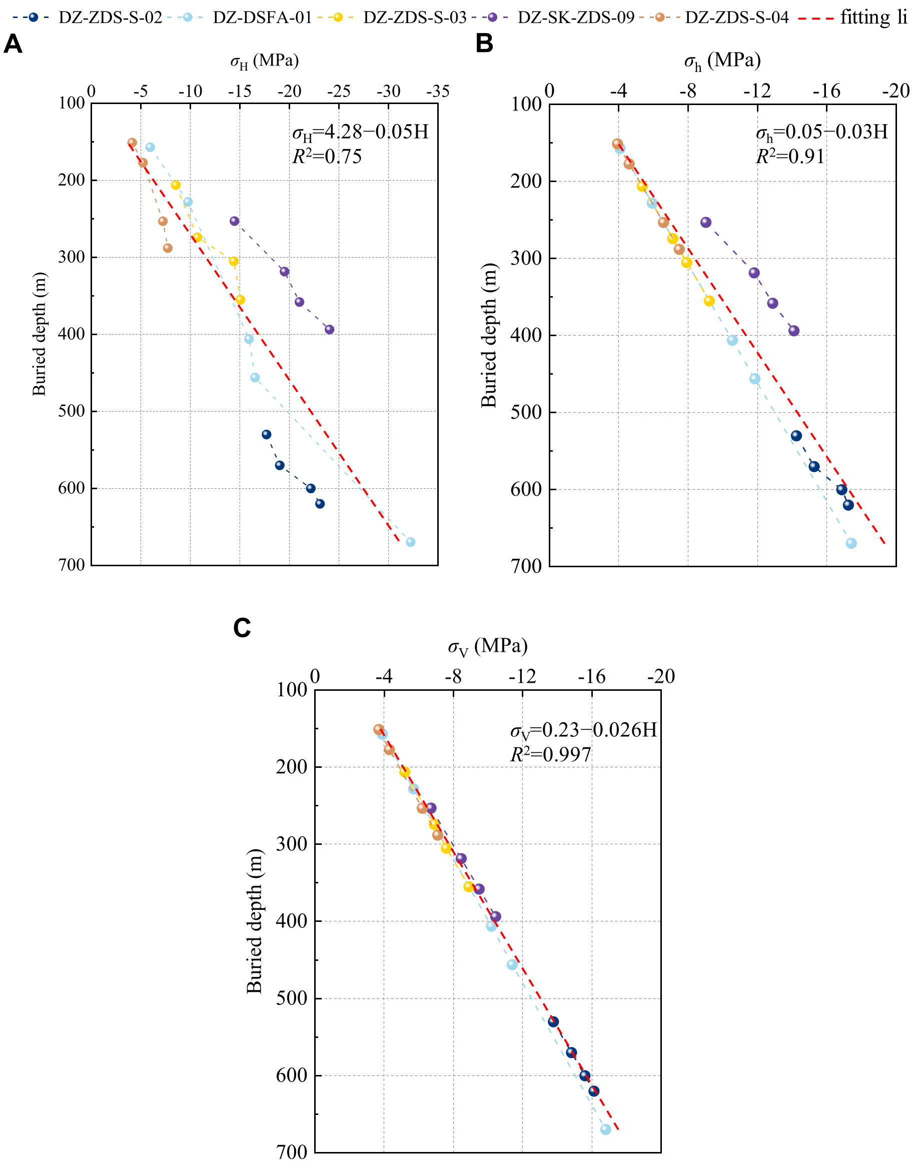

FIGURE 3
Measured *in situ* stress: **(A)** maximum horizontal principal stress; **(B)** minimum horizontal principal stress; **(C)** vertical stress.

04 boreholes are particularly significant. Comparing Figure 2, it can be seen that these three boreholes are located on both sides of the tunnel site area and are far away from the two middle boreholes. Therefore, there are certain differences in the distribution characteristics of *in situ* stress in different local areas.

To further demonstrate the linear relationship between each stress component and the buried depth, Figure 3 also shows the linear fitting results of the measured data. Among them, the linear relationship between σ_V and burial depth (H) is the most significant, and its goodness of fit R^2 reaches 0.997. Secondly, σ_h also has a good linear correlation with buried depth, and the corresponding goodness of fit R^2 is 0.91. In addition, the linear correlation between σ_H and burial depth is the weakest, and the corresponding goodness of fit R^2 is only 0.75.

The buried depth range of the DZ-ZDS-S-02, DZ-DSFA-01, DZ-ZDS-S-03, DZ-SK-ZDS-09, and DZ-ZDS-S-04 boreholes is 530–620 m, 157–670 m, 206–355 m, 253–394 m, and 151–288 m, respectively. The corresponding σ_H range of each borehole is −17.73 ~ −23.08 MPa, −6.02 ~ −32.20 MPa, −8.47 ~ −15.11 MPa, −14.53 ~ −24.06 MPa, and −4.09 ~ −7.72 MPa, respectively, the σ_h range of each borehole is −14.30 ~ −17.32 MPa, −4.11 ~ −17.43 MPa, −5.38 ~ −9.17 MPa, −9.01 ~ −14.06 MPa, and −3.92 ~ −7.46 MPa, respectively, and the σ_V range of each borehole is −13.83 ~−16.12 MPa, −3.90

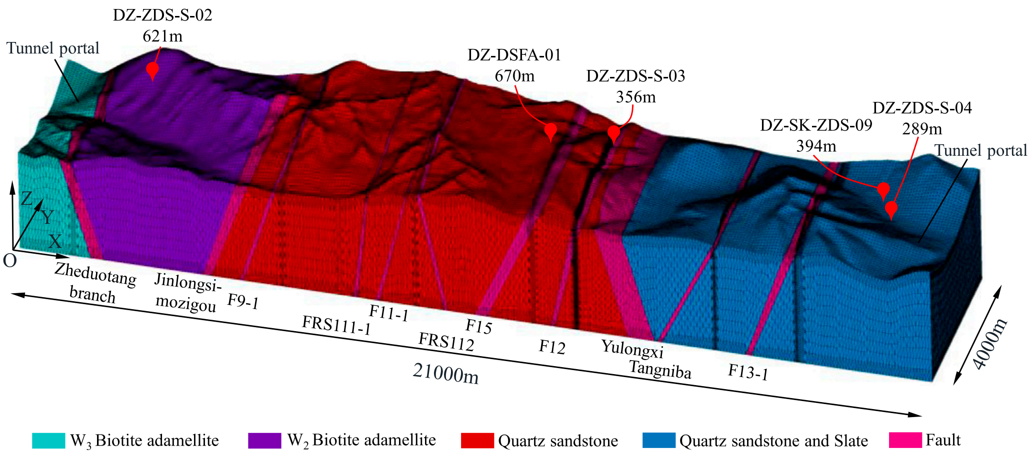

FIGURE 4
Three-dimensional numerical model of the tunnel site area.

TABLE 1 Physical and mechanical parameters of the rock masses.

Rock	Elastic modulus (GPa)	Poisson's ratio	Density (kg/m^3)	Cohesion strength (MPa)	Internal friction angle (°)
W_3 Biotite adamellite	13.00	0.27	2300.00	1.10	45.00
W_2 Biotite adamellite	33.00	0.20	2500.00	2.00	60.00
Quartz sandstone	26.00	0.23	2500.00	1.80	55.00
Quartz sandstone and Slate	22.00	0.24	2450.00	1.60	53.00
Fault	1.50	0.43	2100.00	0.30	35.00

~−16.84 MPa, −5.18 ~−8.91 MPa, −6.74 ~−10.37 MPa, and −3.66 ~ −7.08 MPa, respectively.

The *in situ* stress gradient in the tunnel site can be obtained by dividing the stress increment by the buried depth increment. The calculation indicates that the average increment gradients per 100 m buried depth of σ_H, σ_h, and σ_V are 4.32 MPa, 2.81 MPa, and 2.53 MPa, respectively. In other words, σ_H is 1.54 times σ_h and 1.71 times σ_V. Hence, the *in situ* stress field of the tunnel presents $\sigma_H > \sigma_h > \sigma_V$. This indicates that the horizontal tectonic movement of the strata in this area is strong, and the *in situ* stress is dominated by the horizontal principal stress.

3 Inversion method with optimized fitting conditions

3.1 Inversion principle

Since there is no field condition for measuring *in situ* stress inside the tunnel, the measurement by the hydraulic fracturing method is the only means in the geological exploration stage (Zhang et al., 2014). The principle of the hydraulic fracturing method indicates that its stress components are derived based on elastic assumptions (Pei et al., 2016). That is to say, the measured *in situ* stresses obtained by the hydraulic fracturing method are all elastic stresses. Based on this, the multiple linear regression method using the least squares optimization criterion according to the principle of linear superposition is widely used in the field of *in situ* stress inversion. In short, the inversion principle of the multiple linear regression method is to approximate the observed value through the regression value to solve the regression coefficient. In other words, the residual sum of squares between the regression value and the observed value is minimized based on the least squares method. The regression model of the multiple linear regression method is as follows:

$$\hat{\boldsymbol{\sigma}}_{jk} = a_0 + \sum_{i=1}^{n} a_i \boldsymbol{\sigma}_{jk}^{i} \tag{1}$$

where $\hat{\boldsymbol{\sigma}}_{jk}$ is the j-th regression stress component of the k-th observed point, a_0 is the constant term, n is the total number of

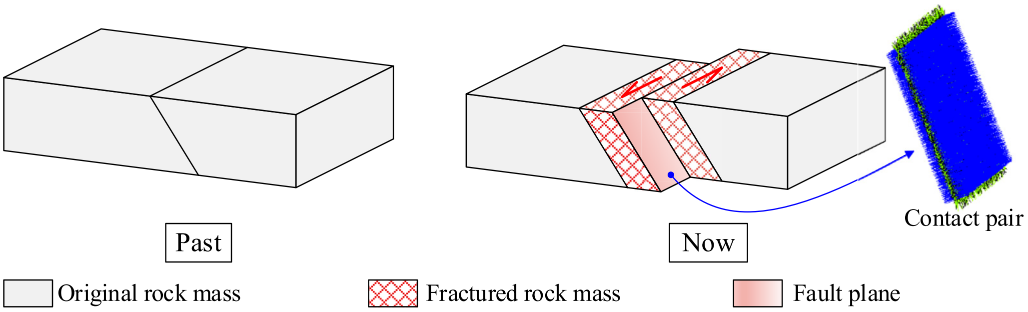

FIGURE 5
Genetic mechanism of the fault: **(A)** original rock mass; **(B)** fault.

TABLE 2 Measured *in situ* stresses after coordinate transformation.

Borehole	σ_x (MPa)	σ_y (MPa)	σ_z (MPa)	τ_{xy} (MPa)	Orientation
DZ-ZDS-S-02	−17.72	−14.28	−13.83	−0.38	N67°W
	−18.96	−15.32	−14.76	−0.42	
	−22.11	−16.91	−15.59	−0.43	
	−23.02	−17.34	−16.12	−0.67	
DZ-DSFA-01	−5.87	−4.06	−3.87	0.28	N51°W
	−9.74	−5.96	−5.73	0.39	
	−15.88	−10.59	−10.16	0.33	
	−-16.26	−12.11	−11.39	1.12	
	−30.83	−18.83	−16.84	4.41	
DZ-ZDS-S-03	−8.41	−5.50	−5.22	0.58	N50°W
	−10.62	−7.23	−6.93	0.63	
	−14.14	−8.26	−7.61	1.38	
	−14.85	−9.39	−8.90	0.92	
DZ-SK-ZDS-09	−12.79	−10.65	−6.67	2.53	N28°W
	−17.50	−13.81	−8.48	3.38	
	−20.13	−13.83	−9.52	2.59	
	−18.31	−19.88	−10.39	4.91	
DZ-ZDS-S-04	−4.14	−3.87	−3.72	0.03	N52°W
	−5.18	−4.62	−4.28	0.12	
	−7.22	−6.63	−6.16	0.14	
	−7.67	−7.51	−7.13	0.05	

boundary conditions, a_i is the regression coefficient of the i-th boundary condition, and $\boldsymbol{\sigma}_{jk}^{i}$ is the calculated stress.

The residual sum of squares, i.e., $Q = (e_{jk})^2$, between the regression and observed values is as follows:

$$Q = \left(e_{jk}\right)^2 = \sum_{k=1}^{m}\sum_{j=1}^{s}\left(\sigma_{jk}^{m} - a_0 - \sum_{i=1}^{n} a_i \sigma_{jk}^{i}\right)^2, \qquad (2)$$

where m is the total number of observed points, s is the total number of stress components, σ_{jk}^{m} is the measured stress, which is also called observed stress.

Furthermore, the regression coefficient can be obtained by taking the minimum value of the residual sum of squares based on the least squares method. The solution equation is as follows:

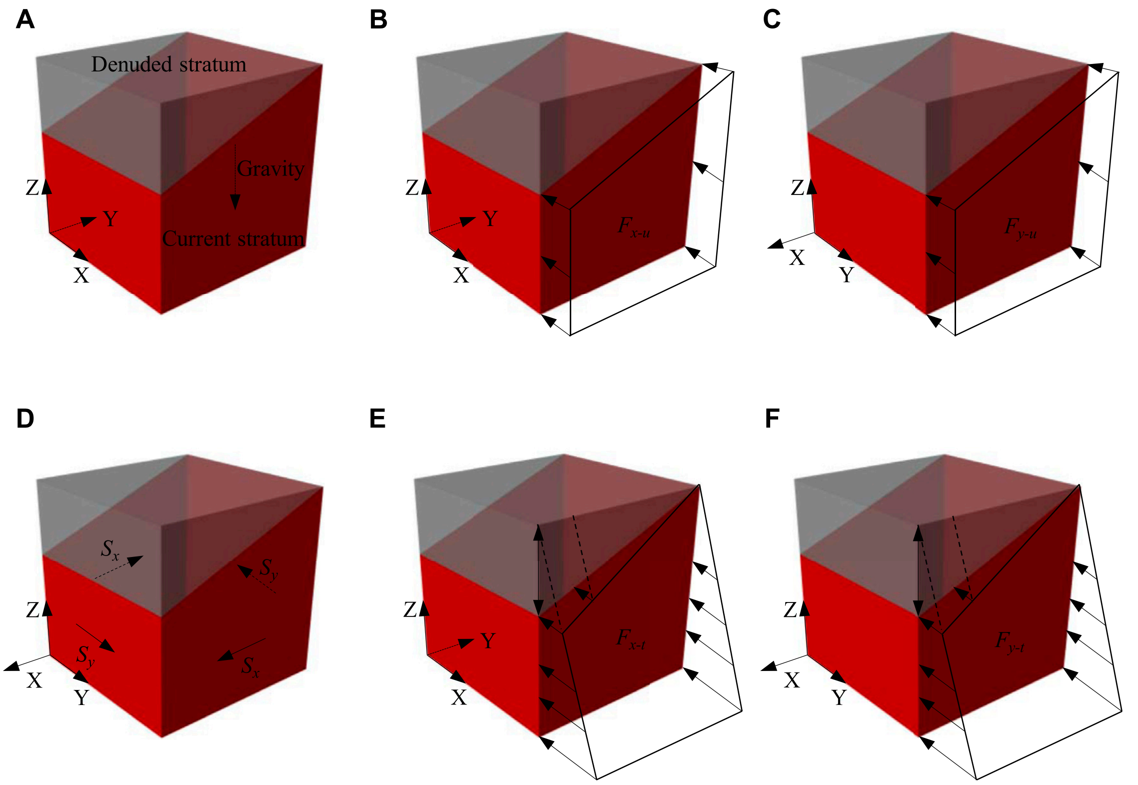

FIGURE 6
Boundary conditions of multiple linear regression method: **(A)** self-weight stress; **(B)** uniform load in X direction; **(C)** uniform load in Y direction; **(D)** shear load in XOY plane; **(E)** triangular gradient load in X direction; **(F)** triangular gradient load in Y direction.

$$\begin{bmatrix} ms & \sum_{k=1}^{m}\sum_{j=1}^{s}\sigma_{jk}^{1} & \sum_{k=1}^{m}\sum_{j=1}^{s}\sigma_{jk}^{2} & \cdots & \sum_{k=1}^{m}\sum_{j=1}^{s}\sigma_{jk}^{n} \\ \cdot & \sum_{k=1}^{m}\sum_{j=1}^{s}\left(\sigma_{jk}^{1}\right)^{2} & \sum_{k=1}^{m}\sum_{j=1}^{s}\sigma_{jk}^{1}\sigma_{jk}^{2} & \cdots & \sum_{k=1}^{m}\sum_{j=1}^{s}\sigma_{jk}^{1}\sigma_{jk}^{n} \\ \cdot & \cdot & \sum_{k=1}^{m}\sum_{j=1}^{s}\left(\sigma_{jk}^{2}\right)^{2} & \cdots & \sum_{k=1}^{m}\sum_{j=1}^{s}\sigma_{jk}^{2}\sigma_{jk}^{n} \\ \cdot & \cdot & \cdot & \cdot & \vdots \\ \cdot & \cdot & \cdot & \cdot & \sum_{k=1}^{m}\sum_{j=1}^{s}\left(\sigma_{jk}^{n}\right)^{2} \end{bmatrix} \times \begin{bmatrix} a_0 \\ a_1 \\ a_2 \\ \vdots \\ a_n \end{bmatrix} = \begin{bmatrix} \sum_{k=1}^{m}\sum_{j=1}^{s}\sigma_{jk} \\ \sum_{k=1}^{m}\sum_{j=1}^{s}\sigma_{jk}^{1}\sigma_{jk} \\ \sum_{k=1}^{m}\sum_{j=1}^{s}\sigma_{jk}^{2}\sigma_{jk} \\ \vdots \\ \sum_{k=1}^{m}\sum_{j=1}^{s}\sigma_{jk}^{n}\sigma_{jk} \end{bmatrix}, \tag{3}$$

where the left matrix is a symmetric matrix.

The regression model representing the *in situ* stress field in the tunnel site area can be obtained by putting (a_0, a_i) solved in Eqn. 3 into Eqn. 1.

The multiple linear regression method has the characteristics of high computational efficiency and unique output solution, so it is widely used in engineering. However, two issues are not clearly agreed upon in the practical application of this method. One is that the boundary conditions of the calculation conditions have not been unified, and the other is that multiple linear regression can be performed even if the constant term a_0 is deleted. Engineering practices show that these two issues are very likely to impact the inversion accuracy. Therefore, the multiple linear regression method urgently needs to be improved in these two aspects.

3.2 Three-dimensional numerical model

Import the geological plan of the tunnel site area into Surfer software to obtain the three-dimensional coordinate information of the surface. Input this information into ANSYS finite element

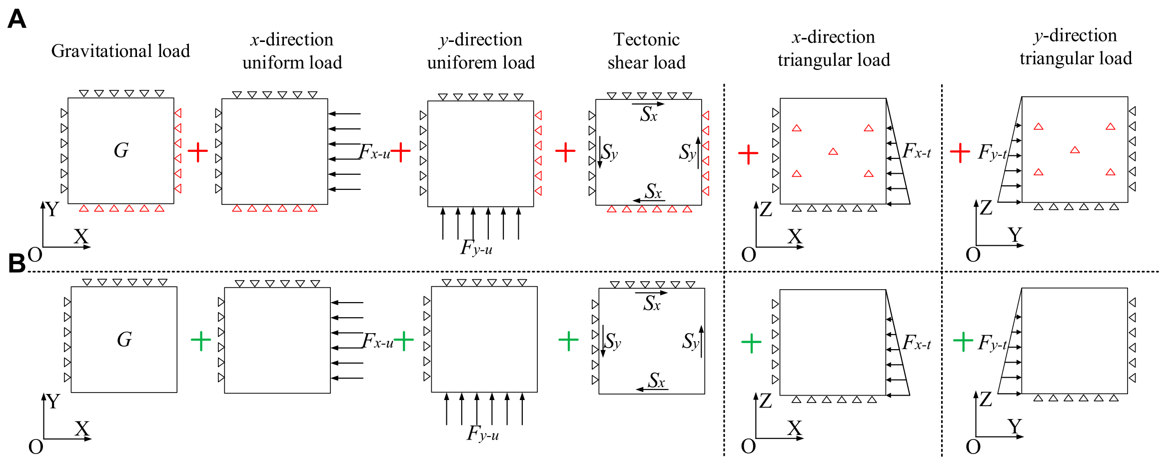

FIGURE 7
Linear superposition principle in multiple linear regression method: **(A)** not unified displacement constraints; **(B)** unified displacement constraints.

software to establish the top surface of the model. The *Z* direction of the model includes the range of 3000 m below the tunnel portal, the Y direction is 4000 m, and the X direction is 21,000 m. As shown in Figure 4, the tunnel axis is basically located in the central area of the three-dimensional numerical model. In order to avoid the deformed grid caused by the irregular surface, the grid refinement process is carried out in some local areas. In the end, the total number of meshes exceeds six million. The physical and mechanical parameters of rock mass were derived from geological exploration data, as shown in Table 1. Literature researches shows that the value range of rock mass parameters around tunnel areas in previous studies is basically consistent with that in Table 1 (Meng et al., 2021; Zhou et al., 2022). In addition, these rock mass parameters are generally consistent with the recommended values in the Code for Design of Railway Tunnel (National Railway Administration of PRC 2017).

For the fault simulation method in the numerical model, the Boolean operation was firstly used to cut the model to form the impact area of the fault fracture zone. Then, the following assumptions were made on the mechanical parameters and contact relationship of the fault based on its genesis. Taking strike-slip faults as an example, Figure 5 shows the genetic mechanism of the fault. When the stress difference exceeds the strength level, the original rock mass begins to fracture. A fault plane, i.e., the fault plane where the two fault walls slide relative to each other, is gradually formed with the development of micro-fractures. Once the fault plane is formed and the stress difference exceeds the frictional resistance, the two fault walls begin to slide relative to each other, forming a fault. With the sliding of the fault, the surrounding rock mass is fractured under the action of friction and shear (Li, 2022). Based on the above mechanism, it was first assumed that the closer to the fault plane, the more fragmented the rock mass. Then the physical and mechanical parameters of the rock mass inside the fault satisfy Eqn. 4.

$$p_L = p_{fp} + \alpha L, \tag{4}$$

where p_L is the physical and mechanical parameter of the rock mass L m away from the fault plane, p_{fp} is the physical and mechanical parameter at the fault plane, $\alpha = p_o - p_{fp}/W$ is the gradient of the physical and mechanical parameters, p_o is the physical and mechanical parameter of the original rock mass, and W is the impact range of the fault.

Secondly, it was assumed that the fault plane was located in the middle of the fractured rock mass (Li et al., 2017), and its frictional constitutive relation adopted the Coulomb friction-slip criterion.

$$\frac{\sigma_1 - P_0}{\sigma_3 - P_0} = \left(\sqrt{1+\mu^2} + \mu\right)^2, \tag{5}$$

where σ_1 and σ_3 are the first principal stress and the third principal stress, respectively, μ is the friction coefficient of the fault plane, P_0 is the pore pressure.

The contact pair in ANSYS software was used to simulate the above fault frictional relationship, shown in Figure 5B.

3.3 Accuracy improvement effect for unifying boundary condition

Due to the coordinate system of the measured stress being different from that of the three-dimensional numerical model, the coordinate system of the measured stress needs to be

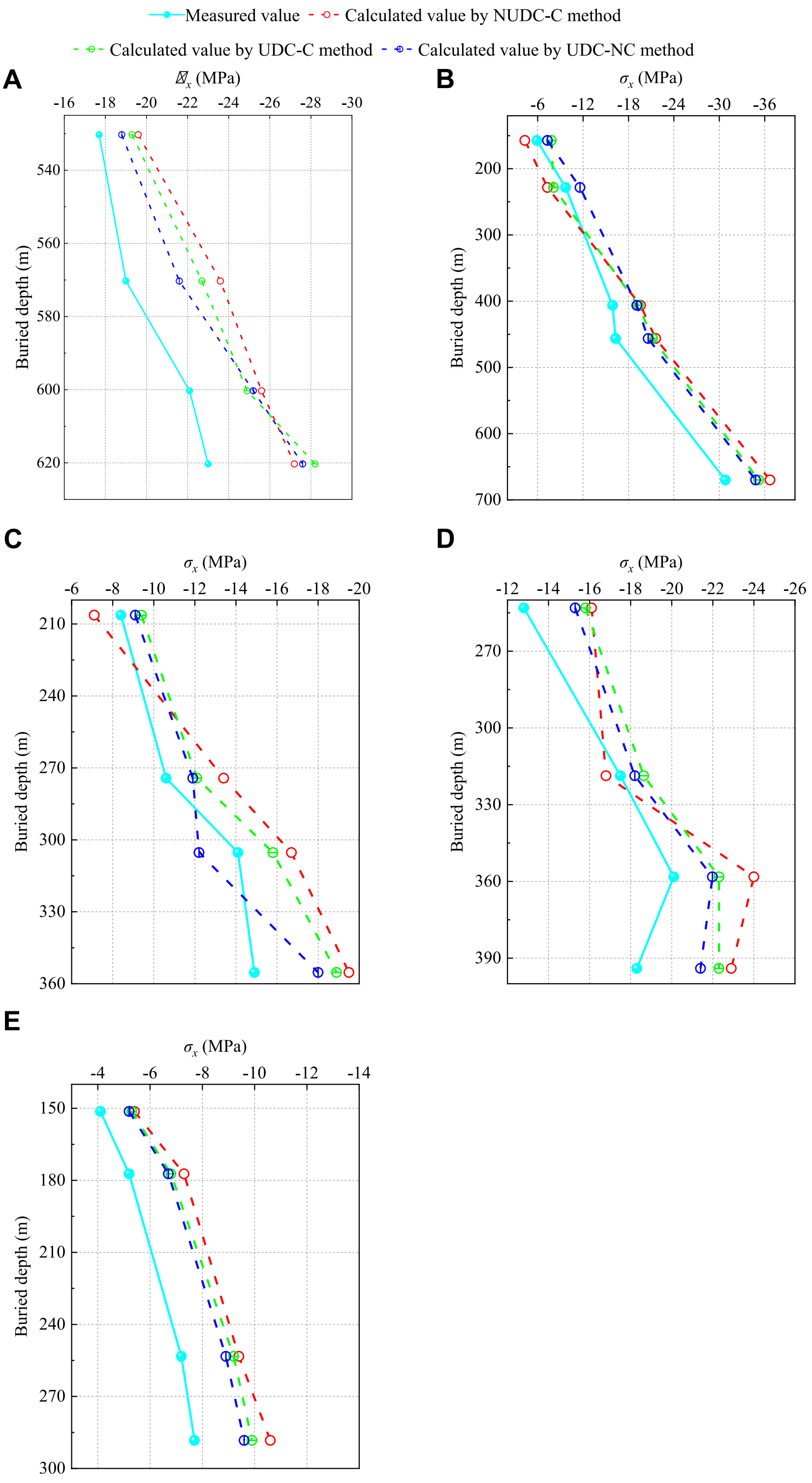

FIGURE 8

Comparison of the measured values and the inversion values: **(A)** DZ-ZDS-S-02 borehole; **(B)** DZ-DSFA-01 borehole; **(C)** DZ-ZDS-S-03 borehole; **(D)** DZ-SK-ZDS-09 borehole; **(E)** DZ-ZDS-S-04 borehole.

TABLE 3 Statistical indicators of σ_x for different inversion methods.

Indicator	NUDC-C method	UDC-C method	UDC-NC method
δ_r	23.9%	20.1%	17.4%
VAF	95.6%	96.3%	97.2%
RMSE	3.4	2.9	2.5
CIA	3.683	3.138	2.702

TABLE 4 Overall statistical indicators of the stress value for different inversion methods.

Indicator	NUDC-C method	UDC-C method	UDC-NC method
δ_r	21.3%	18.0%	16.4%
VAF	94.5%	95.5%	96.3%
RMSE	2.6	2.3	2.1
CIA	2.868	2.525	2.301

TABLE 5 Overall statistical indicators of the stress orientation for different inversion methods.

Indicator	NUDC-C method	UDC-C method	UDC-NC method
δ_r	25.2%	18.1%	15.9%
VAF	92.9%	91.1%	99.1%
RMSE	12.1	10.1	7.3
CIA	12.423	10.370	7.468

transformed before inversion. The coordinate transformation formula in elastic mechanics is as follows:

$$\sigma_{1'q'} = \alpha_{1'p}\alpha_{q'q}\sigma_{pq} \tag{6}$$

$$\sigma_{2'q'} = \alpha_{2'p}\alpha_{q'q}\sigma_{pq} \tag{7}$$

$$\sigma_{3'q'} = \alpha_{3'p}\alpha_{q'q}\sigma_{pq} \tag{8}$$

where $1'$, $2'$, and $3'$ are, x', y', and z', respectively, and $p, q = x, y, z$.

The measured stress after coordinate transformation is shown in Table 2.

Apply boundary conditions simulating self-weight and different tectonic actions to the numerical model to obtain the calculated stress, and then use the inversion principle to obtain the regression model of the *in situ* stress field in the tunnel site area. Common boundary conditions include self-weight stress (Figure 6A), 1 MPa uniform load in the X direction (Figure 6B), 1 MPa uniform load in the Y direction (Figure 6C), unit shear load in the XOY plane (Figure 6D), triangular gradient load in the X direction (Figure 6E), and triangular gradient load in the Y direction (Figure 6F). Among them, the XOY plane adopts the method of forced displacement to simulate the shear effect of plane structure (Meng et al., 2021), and the triangular load is applied with a gradient of 1 kPa/m.

The principle of linear superposition has strict preconditions, one of which is that the material must satisfy Hooke's law, i.e., the mechanical constitutive model of the material is linear elastic. The second is that the boundary conditions of each load condition need to be consistent. In this way, the stress superposition value of each load condition can be equal to the stress value after all loads are applied simultaneously. However, due to the failure to strictly adhere to the boundary requirements of the linear superposition principle, the error of the multiple linear regression method will increase in practical applications. Specifically, the boundary conditions in Figure 6 were transformed into those in Figure 7A (Li et al., 2015). It can be seen from Figure 7A that the displacement constraints under each calculation condition are different. Nevertheless, the essential requirement of the linear superposition principle is that the displacement constraints of each calculation condition need to be consistent. The main reason for this phenomenon is that some scholars assume that the opposite boundary is fixedly

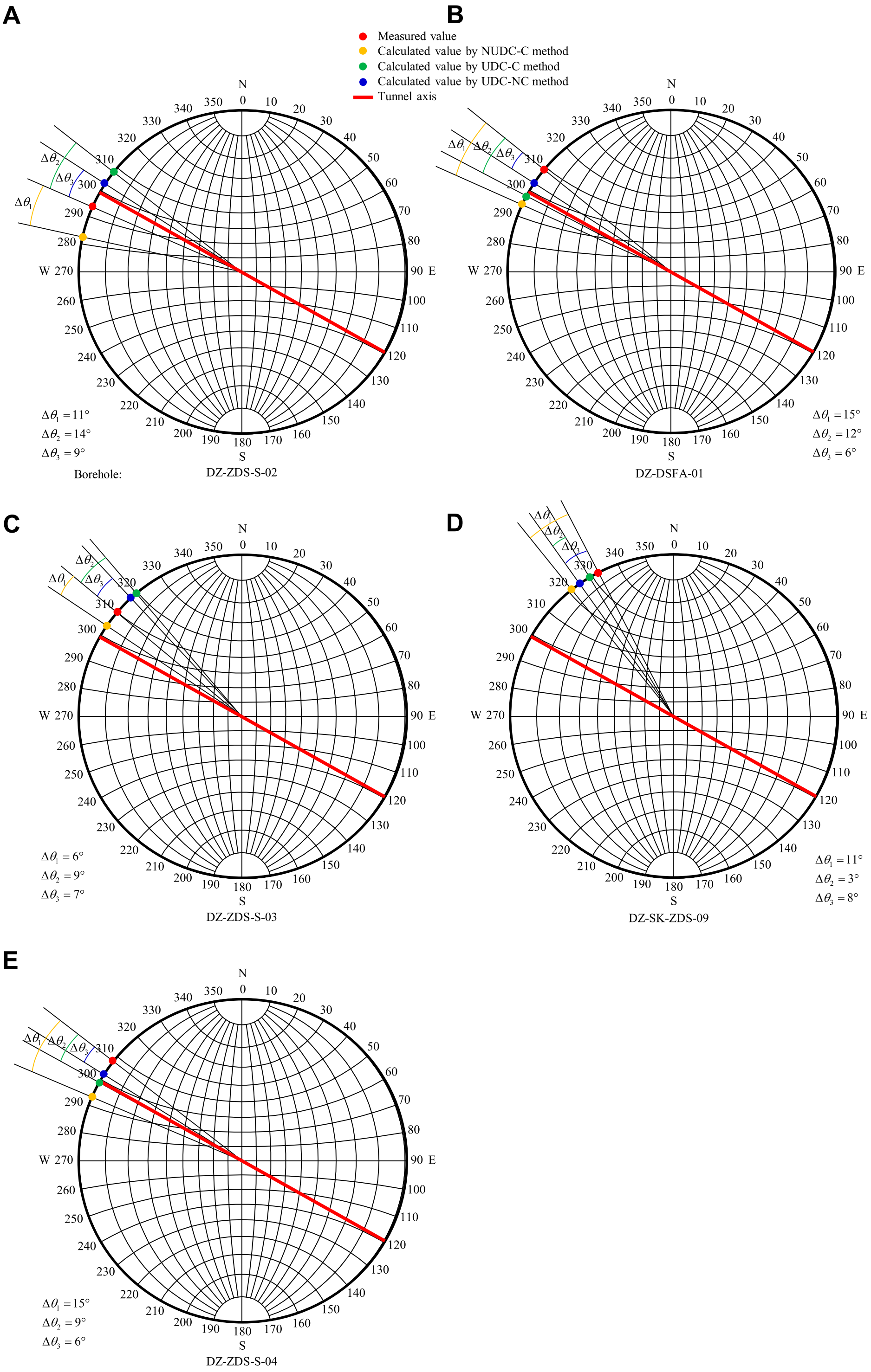

FIGURE 9
Comparison of the measured orientations and the inversion orientations: **(A)** DZ-ZDS-S-02 borehole; **(B)** DZ-DSFA-01 borehole; **(C)** DZ-ZDS-S-03 borehole; **(D)** DZ-SK-ZDS-09 borehole; **(E)** DZ-ZDS-S-04 borehole.

TABLE 6 Comprehensive CIA indicators for different inversion methods.

Indicator	NUDC-C method	UDC-C method	UDC-NC method
CIA	15.291	12.895	9.769

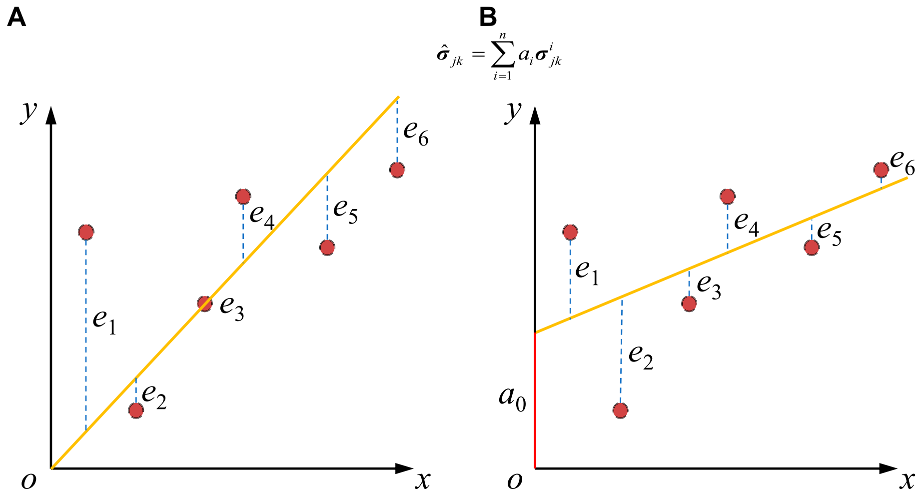

FIGURE 10
Influence of the constant term on data fit: **(A)** not contain a constant term; **(B)** contain a constant term.

constrained when applying tectonic loads (Meng et al., 2020; Zhou et al., 2022). Then, the boundary conditions strictly following the linear superposition principle are shown in Figure 7B. It can be seen from Figure 7B that the displacement constraint conditions of all calculation conditions are consistent. The displacement constraint range of each working condition includes a boundary surface parallel to the X direction, a boundary surface parallel to the Y direction, and the bottom surface.

In order to verify the optimization effect of unified displacement constraints condition on the inversion accuracy, the regression models of two boundary types were solved according to the principle of multiple linear regression. Eqn .9 corresponds to the boundary condition in Figure 7A, i.e., not unified displacement constraints (NUDC-C method), and Eqn. 10 corresponds to the boundary condition in Figure 7B, i.e., unified displacement constraints (UDC-C method). Among them, the last C at the abbreviation represents whether the regression model has a constant term, which will be discussed in the next section.

$$\sigma_{jk}^{\mathrm{NUDC-C}} = 1.40 + 0.92\sigma_{jk}^{g} - 5.36\sigma_{jk}^{x-u} + 10.78\sigma_{jk}^{y-u} + 5.99\sigma_{jk}^{xoy} + 3.31\sigma_{jk}^{x-t} + 2.67\sigma_{jk}^{y-t}, \tag{9}$$

$$\sigma_{jk}^{\mathrm{UDC-C}} = 1.17 + 0.89\sigma_{jk}^{g} - 3.87\sigma_{jk}^{x-u} + 13.26\sigma_{jk}^{y-u} + 10.03\sigma_{jk}^{xoy} + 1.96\sigma_{jk}^{x-t} + 2.01\sigma_{jk}^{y-t}, \tag{10}$$

where $\sigma_{jk}^{\mathrm{NUDC-C}}$ and $\sigma_{jk}^{\mathrm{UDC-C}}$ are the regression stresses solved by the NUDC-C and UDC-C methods, respectively, σ_{jk}^{g} is the calculated stress under self-weight, σ_{jk}^{x-u} and σ_{jk}^{y-u} are the calculated stresses under the uniform load in the X and Y directions, respectively, σ_{jk}^{xoy} is the calculated stress under the shear load in the XOY plane, and σ_{jk}^{x-t} and σ_{jk}^{y-t} are the calculated stresses under the triangular load in the X and Y directions, respectively.

Due to space limitations, only σ_x is selected to show the inversion effects of the two methods, as shown in Figure 8. In addition, their inversion accuracies of all stress components at all measuring points are listed in Table 4 and Table 5. On this basis, the regression orientation of σ_{H} at the observed point can be solved by Eqs. 11, 12; Figure 9 shows the inversion effects of the two methods on orientation.

$$\left\{\begin{matrix}\sigma_{\mathrm{H}}\\ \sigma_{\mathrm{h}}\end{matrix}\right. = \frac{\sigma_x+\sigma_y}{2} \pm \sqrt{\left(\frac{\sigma_x+\sigma_y}{2}\right)^2 + \left(\tau_{xy}\right)^2}, \tag{11}$$

$$tan\,\theta = \frac{(\sigma_{\mathrm{H}}-\sigma_x)}{\tau_{xy}}, \tag{12}$$

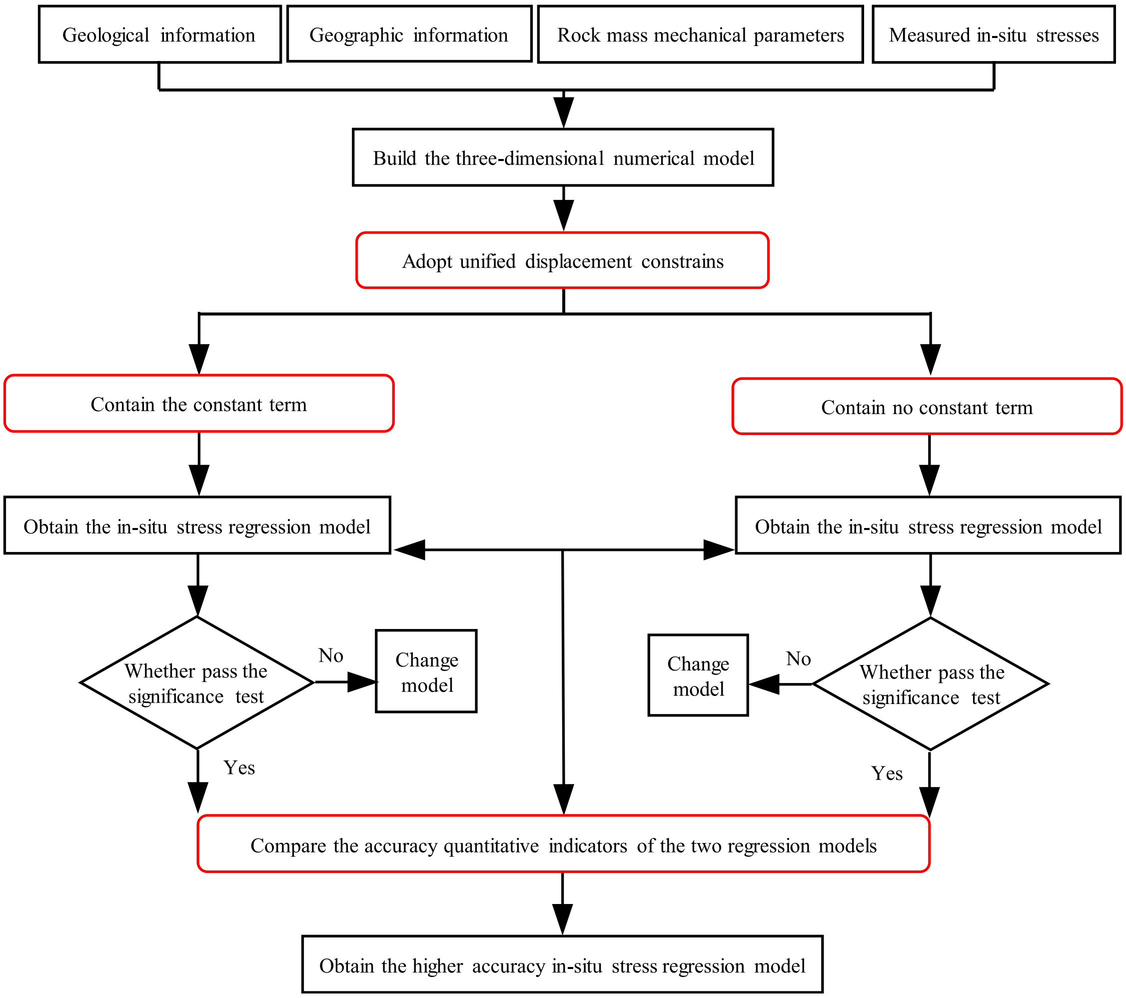

FIGURE 11
Optimized process of the *in situ* stress inversion.

where θ is the angle between σ_H and X-axis.

It can be seen from Figure 8 that the inversion results of the NUDC-C method and the UDC-C method generally maintain a consistent distribution law with the measured values. However, especially at DZ-ZDS-S-03, DZ-SK-ZDS-09, and DZ-ZDS-S-04 boreholes, the distribution law of the inversion results of the UDC-C method is more similar to the measured values. At the same time, the absolute error of the UDC-C method is smaller than that of the NUDC-C method for all other measuring points except for the measuring points with 620 m buried depth in the DZ-ZDS-S-02 borehole, and 319 m buried depth in the DZ-SK-ZDS-09 borehole. Figure 9 also shows that the inversion effect of the UDC-C method is better than that of the NUDC-C method. Except for the DZ-ZDS-S-02 and DZ-ZDS-S-03 boreholes, where the absolute error of the UDC-C method increases by 3°, the absolute errors of the other boreholes decrease significantly. For example, from the NUDC-C method changed to the NDC-C method, the absolute error of the DZ-DSFA-01 borehole is reduced from 15° to 12°, and that of the DZ-SK-ZDS-09 borehole is reduced from 11° to 3°, and that of the DZ-ZDS-S-04 borehole is reduced from 15° to 9°.

Furthermore, the statistical indicators, including the relative error (δ_r), the statistical analysis performance indicators of ANOVA (VAF), and the root mean square (RMSE), are used to comprehensively evaluate the accuracy level of each inversion method (She et al., 2022). Their calculation formulas are shown in Eqs. 13–15, respectively. Among them, the smaller the relative error, the larger the VAF, and the smaller the RMSE, indicating the higher the inversion accuracy. According to this principle, the comprehensive evaluation indicator, i.e., comprehensive inversion accuracy (CIA), can be obtained by normalizing the three statistical indicators and superimposing them. The CIA indicator can be calculated by Eqn. 16.

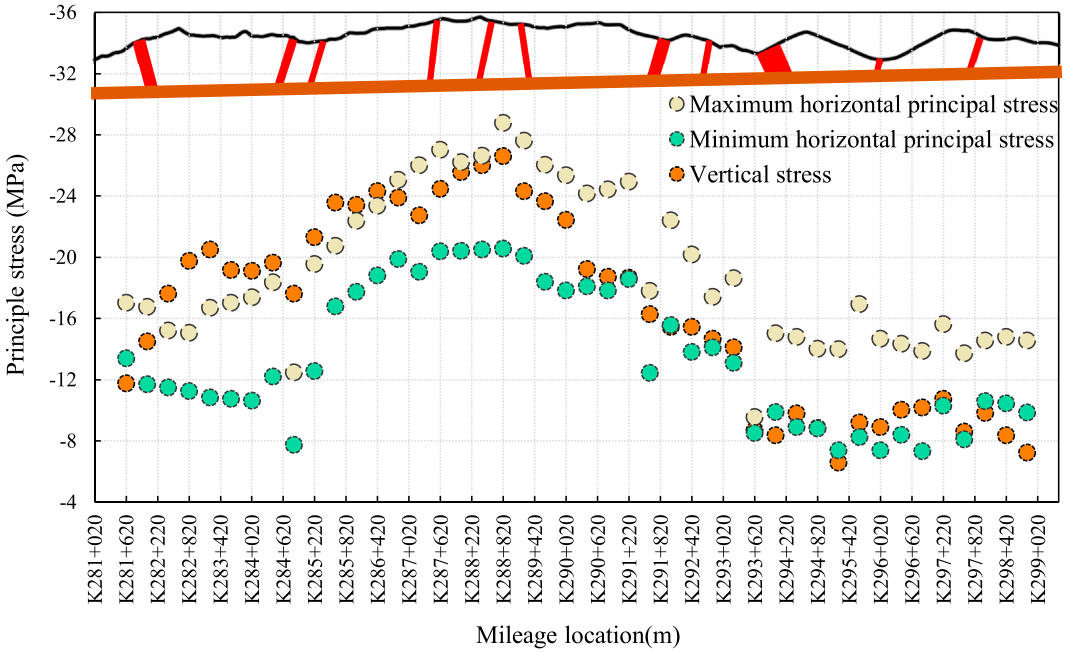

FIGURE 12
Distribution of the *in situ* stress along tunnel axis.

$$\delta_r = \frac{\left|\sigma_{jk}^m - \hat{\sigma}_{jk}\right|}{\left|\sigma_{jk}^m\right|} \times 100\% \qquad (13)$$

$$VAF = \left(1 - \frac{Variance\left(\sigma_{jk}^m - \hat{\sigma}_{jk}\right)}{Variance\left(\sigma_{jk}^m\right)}\right) \times 100\% \qquad (14)$$

$$RMSE = \sqrt{\frac{1}{N}\sum_{i=1}^{N}\left(\sigma_{jk}^m - \hat{\sigma}_{jk}\right)^2}, \qquad (15)$$

where N is the total number of samples.

$$\begin{aligned} CIA &= CIA_{value} + CIA_{orientation} \\ &= \left[\delta_r + (1 - VAF) + RMSE\right]_{value} + \left[\delta_r + (1 - VAF) + RMSE\right]_{orientation} \end{aligned}, \qquad (16)$$

where CIA_{value} refers to the comprehensive inversion accuracy of the stress value, and $CIA_{orientation}$ refers to the comprehensive inversion accuracy of the stress orientation.

Table 3 lists the statistical indicators of σ_x for different inversion methods. It can be seen that all indicators of the UDC-C method are superior to the NUDC-C method. For example, δ_r decreases from 23.9% to 20.1%, VAF increases from 95.6% to 96.3%, and RMSE decreases from 3.4 to 2.9. Finally, the CIA indicator decreases from 3.683 to 3.138. In addition, Table 4 and Table 5 list the statistical indicators of all inversion results of the stress value and orientation, respectively. The UDC-C method outperforms the NUDC-C method in all statistical indicators except the VAF indicator of stress orientation. Based on this, calculate the total CIA indicator of stress value and orientation using Eqn. 16. The comprehensive CIA indicators of the UDC-C method and NUDC-C method are 12.895 and 15.291, respectively (Table 6). To sum up, these data all show that the inversion accuracy is improved after unifying the displacement constraints.

3.4 Effect of constant term on accuracy

The multiple linear regression method also has an uncertain factor in the data fitting: whether the regression model should contain the constant term a_0. Traditional practice generally includes the constant term a_0 (Li et al., 2015; Meng et al., 2021; Zhou et al., 2022), in which case the regression model is Eqn. 1. However, some regression models do not contain the constant term (Figueiredo et al., 2014; Meng et al., 2020; Xu et al., 2021), in which case the regression model is Eqn. 17. In fact, whether to include a constant term is just a matter of choice between the two fitting methods. However, this choice will likely affect the accuracy level of the inversion results. Figure 10 shows the effect of the constant term on the data fit. Obviously, the sum of the errors in Figure 10A, i.e., does not contain a constant term, and that in Figure 10B, i.e., contains a constant term, are probably not equal. Moreover, it is impossible to know in advance which method is more accurate. Therefore, it is necessary to judge whether the constant term should be included before determining the final regression model. Based on this, taking

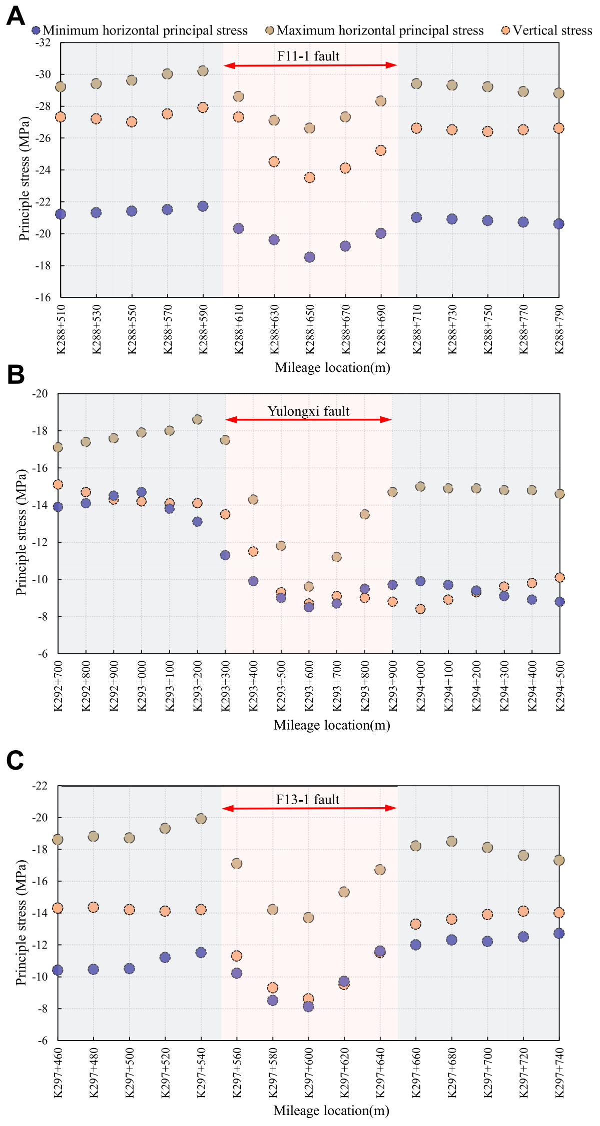

FIGURE 13
Distribution characteristics of *in situ* stress value inside and outside the fault: **(A)** F11-1 fault; **(B)** Yulongxi fault; **(C)** F13-1 fault.

the model with the unified displacement constraints as the standard, the accuracy difference between the inversion methods with a constant term (UDC-C method) and with no constant term (UDC-NC method) is further discussed.

$$\hat{\boldsymbol{\sigma}}_{jk} = \sum_{i=1}^{n} a_i \boldsymbol{\sigma}_{jk}^{i} \tag{17}$$

According to the same inversion principle, the data fitting is performed after removing the constant term, and the obtained regression model is as follows:

$$\sigma_{jk}^{\mathrm{UDC-NC}} = 1.06\sigma_{jk}^{g} - 1.73\sigma_{jk}^{x-u} + 16.11\sigma_{jk}^{y-u} + 9.72\sigma_{jk}^{xoy} + 3.50\sigma_{jk}^{x-t} + 4.06\sigma_{jk}^{y-t} \tag{18}$$

The inversion results of σ_x by the UDC-NC method are shown in Figure 8. The absolute errors of all other measuring points reach the smallest, except for the measuring points with 600 m and 620 m buried depths in the DZ-ZDS-S-02 borehole and 228 m buried depth in the DZ-DSFA-01 borehole. In addition, the statistical indicators of σ_x in Table 3 also show that the UDC-NC method has the highest inversion accuracy, and its CIA indicator is 2.702. At the same time, Figure 9 shows that the inversion method with no constant term gives the highest inversion accuracy for the orientation of σ_{H}. For example, the absolute errors of DZ-ZDS-S-02, DZ-DSFA-01, DZ-ZDS-S-03, and DZ-ZDS-S-04 are 9°, 6°, 7°, and 6°, respectively, all reaching the minimum value. Table 4, Table 5, and Table 6 list the statistical indicators of all inversion results of the UDC-NC method. Regardless of stress value or orientation, the δ_r, VAF, and RMSE all reach the minimum value. Among them, the overall CIA indicator of the stress value, stress orientation, and comprehensive index of the UDC-NC method are 2.301, 7.468, and 9.769, respectively, which are the minimum values among the three methods. This shows that the *in situ* stress inversion accuracy using the regression model with no constant term is much higher.

It should be emphasized that although the inversion accuracy of the UDC-NC method in this tunnel engineering is higher than that of the UDC-C method, it does not prove that the fitting method with no constant term will obtain more accurate inversion results. In fact, according to the fitting principle in Figure 10, the influence of the constant term on the inversion accuracy is random. In other words, higher inversion accuracy may appear in regression models with no constant terms or regression models with a constant term. Therefore, it is recommended that the effect of the constant term on the inversion error must be discussed before determining the regression model.

Based on the above improvement measures for the multiple linear regression method in terms of fitting conditions, the optimized process of *in situ* stress inversion is summarized as follows (Figure 11). The first step is to collect the geological information, geographic information, rock mass mechanical parameters, and measured *in situ* stresses. The second step is to build a three-dimensional numerical model based on the information. The third step is to keep the displacement constraints of the model consistent under each working condition. The fourth step is to discuss the effect of the constant term on accuracy. The fifth step is to select the regression model with higher inversion accuracy to obtain the *in situ* stress field in the tunnel site area.

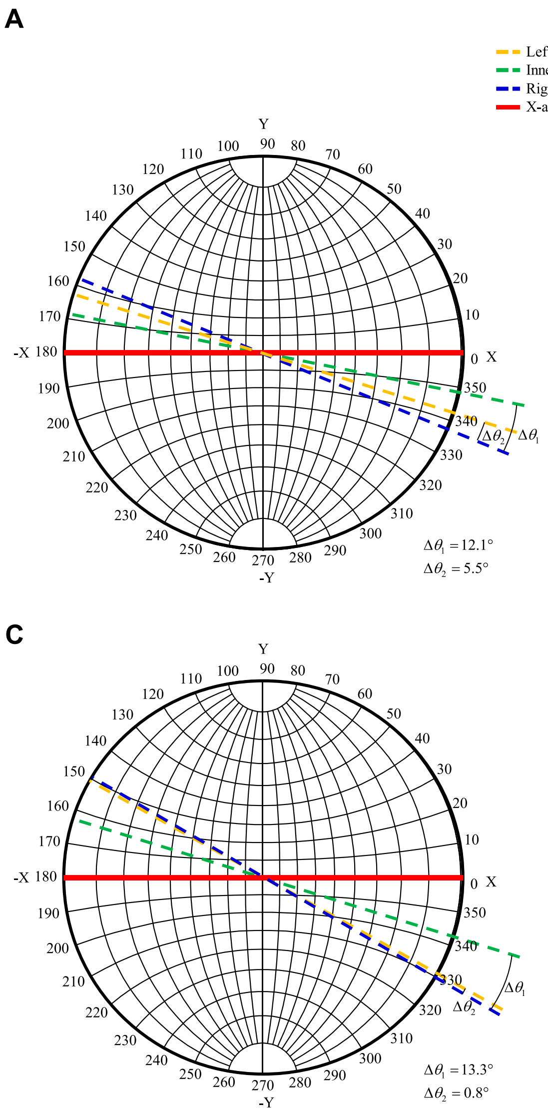

FIGURE 14
Distribution characteristics of *in situ* stress orientation inside and outside the fault: **(A)** F11-1 fault; **(B)** Yulongxi fault; **(C)** F13-1 fault.

4 Distribution characteristics of the *in situ* stress field in fault zone

Affected by the stress concentration effect at the model boundary, the data about 2000 m on both sides of the tunnel axis should be excluded. Figure 12 shows the *in situ* stress distribution in the range of the tunnel axis K281+620 ~ K298+820. From a macro perspective, the σ_H, σ_h, and σ_V are positively correlated with the buried depth of the tunnel. Among them, the vertical stress is the most representative, and its change is basically consistent with the fluctuation of the ground surface and the variation of the buried depth. Specifically, in the range of K285+820 ~ K291+220, the tunnel passes through the maximum buried depth area, and these three stresses all reach the peak range. For example, the range of σ_H is -22.4 MPa ~ -28.8 MPa, the range of σ_h is -17.7 MPa ~ -20.6 MPa, and the range of σ_V is -23.4 MPa ~ -26.6 MPa. At mileage K288+820, the tunnel burial depth reaches the maximum value of about 1215 m, and the corresponding three stresses are -28.8 MPa, -20.6 MPa, and -26.6 MPa, respectively.

On the other hand, their distribution laws are different from the perspective of local areas. Taking the mileage K286+420 as the boundary, the stress distribution law on the left side shows that σ_V is greater than σ_H greater than σ_h, and the stress distribution law on the right shows that σ_H is greater than σ_V greater than σ_h. In the range of K281+620 ~ K286+420, the range of σ_H, σ_h, and σ_V is -12.5 MPa ~ -23.4 MPa, -7.7 MPa ~ -18.8 MPa, and -17.6 MPa ~ -24.3 MPa, respectively, and in the range of K286+420 ~ K298+820, the range of σ_H, σ_h, and σ_V is -13.9 MPa ~ -28.8 MPa, -7.3 MPa ~ -20.6 MPa, and -10.2 MPa ~ -26.6 MPa, respectively. This shows that the stress distribution characteristics of ultra-long tunnels are not invariant, and there are significant differences between their local areas.

In addition, Figure 12 also shows that there are large fluctuations in stress near the fault. This phenomenon is particularly significant in mileage K284+820 and mileage K291+620. For example, at mileage K284+820, the σ_H, σ_h, and σ_V are reduced from -19.6 MPa, -12.5 MPa, and -21.3 MPa to -12.5 MPa, -7.7 MPa, and -17.6 MPa, respectively. At mileage K291+620, the σ_H, σ_h, and σ_V are reduced from -24.9 MPa, -18.5 MPa, and -18.6 MPa to -17.8 MPa, -12.4 MPa, and -16.3 MPa, respectively. This shows that the distribution of faults has a significant disturbance to the *in situ* stress field. On this basis, the three areas in Figure 2 are selected to investigate the disturbance law of the fault distribution to the *in situ* stress field. Among them, compare Area one and Area two to analyze the influence of fault width and compare Area one and Area three to analyze the influence of fault distribution distance.

Select the F11-1 fault in Area one, the Yulongxi fault in Area two, and the F13-1 fault in Area three to analyze the *in situ* stress distribution law in the fault zone (Figure 13). In general, on the outside of the fault, the *in situ* stress slightly increases as it approaches the fault, and inside the fault, the *in situ* stress decreases as it approaches the fault plane. For example, while approaching the fault from outside, σ_H of the F11-1 fault, Yulongxi fault, and F13-1 fault increase by a maximum of 1.1 MPa, 1.5 MPa, and 1.3 MPa, respectively. On the other hand, what is remarkable is that the *in situ* stress inside the fault manifests as a sudden stress drop. Comparing Figures 13A,B, it can be seen that the amplitudes of stress change inside the Yulongxi fault are more evident than that of the F11-1 fault. The maximum amplitude of stress change of the σ_H, σ_h, and σ_V in the F11-1 fault are 3.6 MPa, 3.2 MPa, and 4.4 MPa, respectively. The maximum amplitudes of stress change of the σ_H, σ_h, and σ_V in the Yulongxi fault are 9.0 MPa, 5.6 MPa, and 6.4 MPa, respectively. It can be seen that under the same fault distribution distance, the amplitude of stress change increases by an average of 1.9 times when the width of the fault impact zone increases from 99 m to 614 m. Therefore, the wider the fault, the more significant its disturbance to the *in situ* stress. Comparing Figures 13A,C, it can be seen that the amplitude of stress change inside the F13-1 fault is more evident than that of the F11-1 fault. The maximum amplitudes of stress change of the σ_H, σ_h, and σ_V in the F13-1 fault are 6.2 MPa, 4.6 MPa, and 5.8 MPa, respectively. It can be seen that under the same fault width, the amplitude of stress change increases by an average of 1.5 times when the fault distribution distance increases by about 2.0 times. This shows that the denser the fault distribution, the more minor its disturbance to the *in situ* stress.

Figure 14 shows the variation of σ_H inside and outside the three faults. In Figure 14, the inner center represents the position of the fault plane, and the left and right outer sides are both located at the center of the outer sides of two adjacent faults. It can be seen that the *in situ* stress orientation is deflected between both the outer sides of the fault and between the inside and outside sides. In general, the disturbance of the fault impact zone width and the fault distribution distance on the stress orientation is similar to the disturbance on the stress value. For example, comparing Figures 14A,B, it can be found that the wider the fault impact zone is, the more significant the *in situ* stress orientation changes. $\Delta\theta_1$ and $\Delta\theta_2$ of the F11-1 fault are 12.1° and 5.5°, respectively, while those of the Yulongxi fault are 17.9° and 8.3°, respectively. Comparing Figures 14A,C, it can be found that after the distribution distance between the faults increases, the variation between the inner and outer orientations increases slightly. The $\Delta\theta_1$ of the F13-1 fault increases to 13.3°. Nevertheless, on the other hand, as the distribution distance between faults increases, the orientations of the two outer sides of the fault remain almost unchanged, e.g., $\Delta\theta_2$ is only 0.8°.

5 Conclusion

In this paper, an inversion method with unified displacement constraints was proposed to improve the inversion accuracy. On this basis, the influence of the constant term in the regression model on the inversion accuracy was discussed, and the specific process of the inversion method with optimized fitting conditions was proposed. By using this optimized method, the *in situ* stress field distribution law between the densely distributed faults in the tunnel site area was revealed. The main conclusions are summarized as follows:

1) Combining the statistical indicators with δ_r, VAF, and RMSE, a CIA indicator that can comprehensively evaluate the *in situ* stress inversion accuracy is proposed. The smaller the CIA indicator, the higher the inversion accuracy.
2) The inversion method with unified displacement constraints has been verified can improve the inversion accuracy. Before and after the unification of displacement constraints, the CIA indicators between the measured and inversion values at all measuring points are 15.291 and 12.895, respectively.
3) Whether keep the constant term in the regression model has an impact on the inversion error. Therefore, it is recommended to investigate the effect of the constant term before determining the regression model.
4) From the outer side of the fault to the inner side, the *in situ* stress increases slightly and then decreases significantly. A significant stress drop develops inside the fault. On the other hand, the wider the fault impact zone, the larger the fault

distribution distance, and the more significant the amplitude of stress change. When the width of the fault impact zone increases from 99 m to 614 m, the maximum amplitude of stress change increases from 4.4 MPa to 9.0 MPa. When the fault distribution distance increases by 2.0 times, the maximum amplitude of stress change increases from 4.4 MPa to 6.2 MPa.

5) Furthermore, the wider the fault impact zone, the greater the deflection of the *in situ* stress orientation between inside and outside the fault. When the width of the fault impact zone becomes wider, the variation between the inner and outer sides increases from 12.1° to 17.9°. In addition, the fault distribution distance has no significant effect on the variation between the inner and outer *in situ* stress orientation. However, after the fault distribution distance increases, the *in situ* stress orientations on the two outer sides of the fault are basically consistent.

Data availability statement

The original contributions presented in the study are included in the article/supplementary material, further inquiries can be directed to the corresponding author.

Author contributions

TL has performed the numerical analysis, data analysis, and draft manuscript. ZC supervised the whole research, performed the data analysis and discussion. ZZ designed the overall structure and innovation and reviewed and did the final editing. YB performed the data processing of some figures and tables.

Funding

This research was supported by the National Natural Science Foundation of China (No. 52008351), the Sichuan Science and Technology Program (No. 2021YJ0539), the project funded by China Postdoctoral Science Foundation (No. 2020TQ0250) and the Fundamental Research Funds for the Central Universities (No. 2682021CX013).

Conflict of interest

TL and YB were employed by the company China Railway 12th Bureau Group Co., Ltd.

The remaining authors declare that the research was conducted in the absence of any commercial or financial relationships that could be construed as a potential conflict of interest.

Publisher's note

All claims expressed in this article are solely those of the authors and do not necessarily represent those of their affiliated organizations, or those of the publisher, the editors and the reviewers. Any product that may be evaluated in this article, or claim that may be made by its manufacturer, is not guaranteed or endorsed by the publisher.

References

Fan, Y., Cui, X. Z., Leng, Z. D., Zheng, J. W., Wang, F., and Xu, X. L. (2021). Rockburst prediction from the perspective of energy release: A case study of a diversion tunnel at jinping II hydropower station. *Front. Earth Sci. (Lausanne).* 9, 711706. doi:10.3389/feart.2021.711706

Figueiredo, B., Cornet, F. H., Lamas, L., and Muralha, J. (2014). Determination of the stress field in a mountainous granite rock mass. *Int. J. Rock Mech. Min. Sci. (1997).* 72, 37–48. doi:10.1016/j.ijrmms.2014.07.017

Han, J., Zhang, H. W., Liang, B., Rong, H., Lan, T. W., Liu, Y. Z., and Ren, T. (2016). Influence of large syncline on *in situ* stress field: A case study of the kaiping coalfield, China. *Rock Mech. Rock Eng.* 49 (11), 4423–4440. doi:10.1007/s00603-016-1039-4

Hu, D., Liang, X. Q., Li, Y. S., Wu, Y. P., and Jiang, L. (2022). Deformation prediction of tunnel-surrounding rock considering the time effect of the viscosity coefficient: A case of an NATM-excavated tunnel. *Front. Earth Sci. (Lausanne).* 10, 843545. doi:10.3389/feart.2022.843545

Li, G., Hu, Y., Li, Q. B., Yin, T., Miao, J. X., and Yao, M. D. (2020a). Inversion method of *in-situ* stress and rock damage characteristics in dam site using neural network and numerical simulation—A case study. *IEEE Access* 8, 46701–46712. doi:10.1109/access.2020.2979024

Li, P., Guo, Q. F., Miao, S. J., and Cai, M. F. (2017). Comparisons of *in-situ* stress fields and stability of faults in shallow and deep engineering areas. *J. Harbin Inst. Technol.* 49 (9), 10–16. doi:10.11918/j.issn.0367-6234.201608057

Li, X. P., Zhou, X. J., Xu, Z. X., Feng, T., Wang, D., Deng, J. H., Zhang, G. Z., Li, C. B., Feng, G., Zhang, R., Zhang, Z. L., and Zhang, Z. T. (2020b). Inversion method of initial *in situ* stress field based on BP neural network and applying loads to unit body. *Adv. Civ. Eng.* 2020, 1–15. doi:10.1155/2020/8840940

Li, X. Y. (2022). Investigation of genetic mechanism of the Shigang fault zone in the Northern Jiangsu basin using physical analog sand-box modeling. *Energy Rep.* 8, 9379–9391. doi:10.1016/j.egyr.2022.07.034

Li, Y., Guo, Y. H., Zhu, W. S., Li, S. C., and Zhou, H. (2015). A modified initial *in-situ* stress inversion method based on FLAC3D with an engineering application. *Open Geosci.* 7 (1), 824–835. doi:10.1515/geo-2015-0065

Liu, Y. X., Zhang, Y. Q., Su, P. D., Zhang, G. Z., Qiu, P., and Tang, L. (2022). Risk prediction of rock bursts and large deformations in YL tunnel of the chongqing–kunming high-speed railway. *Front. Earth Sci. (Lausanne).* 10, 892606. doi:10.3389/feart.2022.892606

Meng, W., and He, C. (2020). Back analysis of the initial geo-stress field of rock masses in high geo-temperature and high geo-stress. *Energies* 13 (2), 363. doi:10.3390/en13020363

Meng, W., He, C., Zhou, Z. H., Li, Y. Q., Chen, Z. Q., Wu, F. Y., et al. (2021). Application of the ridge regression in the back analysis of a virgin stress field. *Bull. Eng. Geol. Environ.* 80 (3), 2215–2235. doi:10.1007/s10064-020-02043-y

National Railway Administration of Prc (2017). *Code for design of Railway tunnel.* Beijing China: China Railway Press.

Ning, Y., Tang, H., Smith, J. V., Zhang, B., Shen, P., and Zhang, G. (2021). Study of the *in situ* stress field in a deep valley and its influence on rock slope stability in Southwest China. *Bull. Eng. Geol. Environ.* 80 (4), 3331–3350. doi:10.1007/s10064-020-02094-1

Pei, Q. T., Ding, X. L., Lu, B., Zhang, Y. T., Huang, S. L., and Dong, Z. H. (2016). An improved method for estimating *in situ* stress in an elastic rock mass and its engineering application. *Open Geosci.* 8 (1), 523–537. doi:10.1515/geo-2016-0047

She, L., Zhang, S. R., Wang, C., Du, M., and Yang, P. (2022). A cutting mechanics model of constant cross-section type disc cutter and its application based on dense core theory. *Int. J. Rock Mech. Min. Sci. (1997).* 150, 105025. doi:10.1016/j.ijrmms.2021.105025

Wang, Z. S., Xiang, H., Wang, L. B., Xie, L., Zhang, Z. G., Gao, L. F., Yan, Z. F., and Li, F. L. (2022). Fracture characteristics and its role in bedrock reservoirs in the Kunbei fault terrace belt of Qaidam basin, China. *Front. Earth Sci. (Lausanne).* 10, 865534. doi:10.3389/feart.2022.865534

Xu, D. P., Huang, X., Jiang, Q., Li, S. J., Zheng, H., Qiu, S. L., Xu, H. S., Li, Y. H., Li, Z. G., and Ma, X. D. (2021). Estimation of the three-dimensional *in situ* stress field around a large deep underground cavern group near a valley. *J. Rock Mech. Geotechnical Eng.* 13 (3), 529–544. doi:10.1016/j.jrmge.2020.11.007

Yuan, D., Zhang, L. B., Liu, X. L., Feng, T., Zhang, G. Z., Xu, Z. X., Wang, Z. W., Yi, X. J., Lin, Z. H., Ren, Y., Zhang, R., and Ren, L. (2022). Influence of the Xianshuihe fault zone on *in situ* stress field of a deep tunnel and its engineering effect. *Front. Earth Sci. (Lausanne).* 10, 886876. doi:10.3389/feart.2022.886876

Zhang, C. Q., Feng, X. T., and Zhou, H. (2012). Estimation of *in situ* stress along deep tunnels buried in complex geological conditions. *Int. J. Rock Mech. Min. Sci. (1997).* 52, 139–162. doi:10.1016/j.ijrmms.2012.03.016

Zhang, D. L., Sun, Z. Y., and Fang, Q. (2022a). Scientific problems and research proposals for Sichuan-Tibet railway tunnel construction. *Undergr. Space* 7, 419–439. doi:10.1016/j.undsp.2021.10.002

Zhang, H., Ouyang, Z. H., Li, T., Liu, S., Yi, H. Y., Wang, H. L., Chen, J. Q., and Li, K. (2022b). An investigation into the mechanism of rock bursts in mines for tunnel-cut isolated areas with multiple stress fields. *Front. Earth Sci. (Lausanne).* 9, 809839. doi:10.3389/feart.2021.809839

Zhang, S. K., and Yin, S. D. (2014). Determination of *in situ* stresses and elastic parameters from hydraulic fracturing tests by geomechanics modeling and soft computing. *J. Pet. Sci. Eng.* 124, 484–492. doi:10.1016/j.petrol.2014.09.002

Zhao, T., Hu, W. G., Zhao, R., Yang, M., Wang, Q., Lin, H. X., Ru, Z. X., Bao, D., and Cao, F. (2021). Present *in-situ* stress distribution characteristics of strike-slip in SH oilfield, Tarim basin. *Arab. J. Geosci.* 14, 1223. doi:10.1007/s12517-021-07552-y

Zhou, Z. H., Chen, Z. Q., He, C., Meng, W., Wu, F. Y., Kou, H., and Yan, J. (2022). *in situ* stress field along the axis of deeply buried tunnel in Southwest China employing the segmented single-borehole inversion method. *Int. J. Geomech.* 22 (6), 04022064. doi:10.1061/(ASCE)GM.1943-5622.0002377